Cement and Concrete Research 41 (2011) 1085–1094

Contents lists available at ScienceDirect

Cement and Concrete Research

journal homepage: http://ees.elsevier.com/CEMCON/default.asp

Monitoring reinforcement corrosion and corrosion-induced cracking using non-destructive x-ray attenuation measurements

Alexander Michel [a], Brad J. Pease [a,*], Mette R. Geiker [a,b], Henrik Stang [a], John Forbes Olesen [a]

[a] Technical University of Denmark (DTU), Department of Civil Engineering, Brovej—Building 118, DK-2800 Kgs. Lyngby, Denmark
[b] Norwegian University of Science and Technology (NTNU), Department of Structural Engineering, Trondheim, Norway

ARTICLE INFO

Article history:
Received 3 December 2010
Accepted 17 June 2011

Keywords:
B. Crack detection
B. EDX
C. Corrosion
D. Reinforcement
Non-destructive testing (NDT)

ABSTRACT

To test the applicability of the x-ray attenuation method to monitor corrosion products as well as the formation and propagation of cracks in cementitious materials, reinforced mortar samples were tested under accelerated corrosion conditions. Experimental results demonstrate x-ray attenuation measurements can track time-dependent development of corrosion products and the subsequent initiation and propagation of corrosion-induced cracks. Also, x-ray attenuation measurements allowed determination of the actual concentration of the corrosion products averaged through the specimen thickness. The total mass loss of steel, obtained by the x-ray attenuation method, was found to be in very good agreement with the mass loss obtained by gravimetric method as well as Faraday's law. Results of the presented experimental approach provide pertinent information for the further development and verification of numerical tools simulating corrosion-induced damage in reinforced concrete.

1. Introduction

Corrosion of reinforcement in reinforced concrete structures is a major deterioration problem causing considerable costs due to durability design, maintenance, and repair needs. Therefore, the development of models to predict the (residual) service life of reinforced concrete structures subjected to corrosion has gained momentum in the past decades. Service life models attempt to describe the initiation and propagation phases of reinforcement corrosion (e.g., Refs. [1–3]) and numerous mechanical models have been developed to describe the subsequent consequences of reinforcement corrosion (i.e., corrosion-induced concrete cracking or spalling) (e.g., Refs. [4–6]). The proposed models can be broadly divided into empirical [4], analytical, [5,7–11], and numerical [6,12–16] models. An initial model to simulate corrosion-induced concrete cracking in Ref. [5] considered only expansion of reinforcement, inducing an internal pressure on the surrounding concrete. This model significantly underestimated the time-to-crack initiation. The initial model was extended and the concept of the "porous" or "diffusion" zone was introduced (e.g., Ref. [8]) to adjust the model to fit experimental data. Later, additional parameters were included in the various models to describe different phenomena related to corrosion-induced concrete cracking, e.g., debonding [12] and creep/shrinkage [14].

The commonly called "diffusion" or "porous" zone is a vital parameter in the proposed corrosion-induced concrete cracking models. The zone describes a region of concrete around the reinforcement which can accommodate expansive corrosion products, delaying stress development in the concrete. This region has a major influence on the predicted time-to-crack initiation and the crack propagation behavior [8,10,15]. These commonly used terms ("diffusion" or "porous" zone) are however potentially misleading and/or confusing. The entire concrete surrounding is porous, not just a certain region in close proximity to the reinforcement. Also, development of solid corrosion products is likely not governed by diffusion alone. Diffusion (i.e., transport of matter due to concentration gradients) may describe the movement of ions present in the concrete pore solution (e.g., Cl^-, Ca^+, K^+) or formed during the corrosion process (e.g., Fe^{2+}, Fe^{3+}) through the concrete pore system. However, solid corrosion products (e.g., Fe_2O_3, Fe_3O_4), which actually induce the internal pressures, precipitate. Therefore, the "diffusion" or "porous" zone is referred to as the corrosion accommodating region (CAR) throughout this paper and is suggested as an alternative term to more accurately describe this region.

Inconsistent values are cited for the CAR, ranging from 0.002 to approximately 0.12 mm in thickness [7]. In some cases, the size of the CAR is "determined" by adjusting the value to provide model outputs in line with experimental results [8,9,15,16]. Other experimental methods (e.g., image correlation [10], acoustic emission [17], ultrasound and thermography [18], etc.) are capable of detecting corrosion-induced damages; however, to date these techniques are not capable of providing simultaneous real-time measurements on the amount and/or location(s) of corrosion products. Experimental

* Corresponding author.
E-mail address: bjp@byg.dtu.dk (B.J. Pease).

0008-8846/$ – see front matter © 2011 Elsevier Ltd. All rights reserved.
doi:10.1016/j.cemconres.2011.06.006

methods to physically measure the thickness of the CAR include cutting, sawing and impregnating samples [10]. These destructive methods are potentially invasive, causing possible movement or washing away of corrosion products and hindering reliable measurements.

2. Research significance

Model predictions of corrosion-induced concrete cracking behavior are heavily dependent upon the size of the corrosion accommodating region (CAR). However, a reliable method to measure the size of the CAR has been lacking. This paper focuses on the application of a non-destructive test method, x-ray attenuation measurements, to monitor the time-dependent development of corrosion products and subsequent corrosion-induced cracking. X-ray attenuation measurements are commonly used to monitor moisture movements in concrete and other porous materials (e.g., Refs. [19–23]). Advantages of the x-ray attenuation technique include the non-invasive nature of the method and the ability to directly measure time-dependent changes in concentration of water (i.e., moisture content). This study investigates the ability of the technique to monitor changes in concentration of corrosion products during reinforcement corrosion and to detect cracking of the surrounding concrete.

3. Experimental approach

To test the applicability of the x-ray attenuation method to monitor the development of corrosion products and cracking behavior in cementitious materials, reinforced mortar samples were tested under accelerated corrosion conditions. All materials and testing methods are described below.

3.1. Materials and specimen preparation

Aalborg Rapid® portland cement (Type 52.5N cement [24]) was used. The mix contained 375 kg/m^3 cement, 1125 kg/m^3 fine aggregates (0–4 mm Class E sand in accordance with Ref. [25]), and had a water-to-cement ratio of 0.50. No chlorides were added to the mix, as corrosion was induced by applying electrical current as described in Section 3.2.1. As reinforcement, a smooth steel rod with 8 mm diameter was embedded in the center of the $4\times6\times15$ cm^3 prism. Fig. 1(a) illustrates the cross-section of the mortar specimen.

After casting, the specimen was stored for 24 hours under a plastic sheet in laboratory conditions (i.e., 20 ± 2°C) and was then demolded. Upon demolding, the specimen was stored under water for additional 24 hours at 20 ± 2°C. The 15 cm long prisms were cut in 2 cm lengths using a water-cooled concrete saw. A lead wire was soldered to the reinforcement to allow for accelerated corrosion. All specimen surfaces, except the top and bottom surfaces (see Fig. 1(a) for orientation), were then sealed with paraffin wax. The top and bottom were left unsealed to allow access of oxygen from the top and moisture/current from the bottom. A second, reference specimen (see Fig. 1(a)) was created using the identical procedure (i.e., materials, specimen dimension, curing, cutting, etc.); however, the reference specimen was un-reinforced and completely sealed with paraffin wax to maintain constant moisture conditions.

3.2. Testing procedures

The experimental set up, given in Fig. 1(a), consisted of the reinforced mortar specimen partially submerged in a tap water bath, a sealed reference sample, and a steel shield. The gap between the reference specimen and the reinforced mortar specimen was covered with a steel shield to prevent a free path for x-ray photons to pass through, which may damage the x-ray equipment. Details concerning the accelerated corrosion and x-ray measurement techniques are discussed in the following sections.

3.2.1. Accelerated corrosion

To impress an electrical current through the counter electrode (ruthenium/iridium mixed metal oxide activated titanium mesh) a DC regulator was used. Electrical connection between the working (reinforcement) and counter electrodes was realized by placing the mortar specimen in tap water (no chlorides were added to the solution). The current density applied during the accelerated test was 250 μA/cm^2. It should be noted that such current densities certainly exceed natural conditions. However, as the focus of this work was to test the applicability of x-ray attenuation technique to detect and monitor corrosion products, the applied current density was considered adequate.

3.2.2. X-ray measurement technique

A GNI x-ray facility located at the Technical University of Denmark [26] was used for x-ray attenuation measurements. Fig. 2 shows the x-ray source (a polychromatic x-ray source), a 252×256 pixel x-ray camera, and a programmable three-axis motion frame for moving the source and camera, which are housed in a shielded, environmentally controlled chamber. The x-ray source excitation settings used were a voltage of 80 keV and a current of 75 μA. The x-ray source was automatically ramped up to these settings over a 200 second "warm-up" period and the x-ray source was allowed to stabilize for 600 seconds prior to recording images.

A single measurement consisted of 20 x-ray camera images recorded with an integration time of 1 second. The intensities measured by individual pixels from the 20 images were summed. So-called dark current images (i.e., x-ray camera images recorded

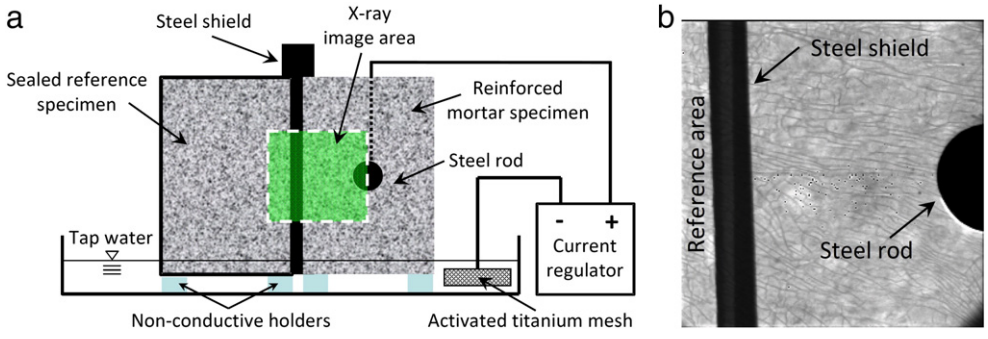

Fig. 1. (a) Experimental set up for accelerated corrosion applying an impressed current with x-ray measurement area indicated, and (b) a typical x-ray image of transmitted intensity showing the steel rod, steel shield, measurement specimen, and the reference area.

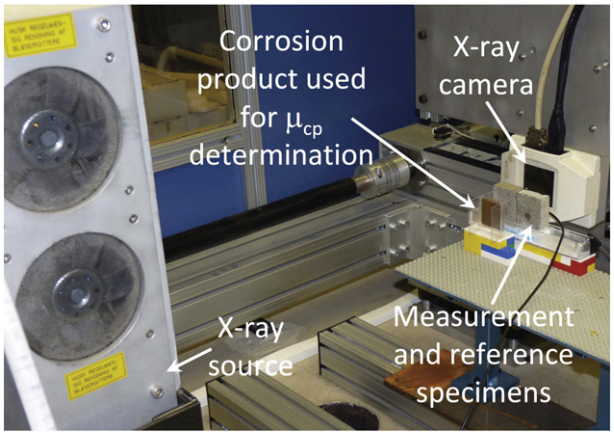

Fig. 2. X-ray attenuation measurement system with experimental setup consisting of the x-ray source and camera along with the specimens. A container filled with corrosion products (Fe_2O_3) was placed in front of the reference specimen to determine linear attenuation coefficient of corrosion products, μ_{cp} (discussed in Section 3.2.4).

while x-ray source is turned off), recorded prior to all x-ray measurements, were subtracted from the measured intensities. Fig. 1 shows the location and size of the measured area along with a typical image captured by the x-ray camera. The area of the reference specimen captured in the x-ray images was used to normalize all images. Before any current was applied to the reinforcement, the specimen was measured three times (i.e., a total of 60 images) in its initial state. After commencing the accelerated corrosion testing, x-ray measurements were recorded every hour, on the hour, for the first 25 hours, followed by measurements every 2 hours until termination of the test at 147 hours. Testing was terminated due to extensive corrosion-induced damage to the mortar. Additional information on the x-ray measurement procedure (i.e., dark current measurements, use of reference samples, etc.) is available in the literature [23,27–29].

As illustrated in Fig. 3, x-ray photons produced by the source interact with the specimen and corrosion products prior to reaching the x-ray camera. The following sections describe the theoretical background of the x-ray attenuation technique and its potential applicability to monitor corrosion of steel reinforcement embedded in cementitious materials.

3.2.3. Theoretical background of x-ray measurement technique

Fig. 3(a) shows the fundamental layout of an x-ray attenuation measurement. The x-ray source produces a polychromatic beam of x-ray photons (i.e., photons with varying energy levels) with a given incident intensity, I_0, which passes through a test specimen with a thickness, t. As the x-ray photons pass through the specimen a portion of the incident intensity, I_0 is attenuated (i.e., absorbed and scattered) and the transmitted intensity, I is recorded by the 64,512 individual pixels in the x-ray camera. The attenuation behavior of a monochromatic x-ray photon (i.e., photons with a single energy level) is described by the Beer–Lambert law (Eq. 1) [20,30]:

$$I = I_0 \cdot e^{-\mu \cdot t} \tag{1}$$

where, μ is the linear attenuation coefficient. The linear attenuation coefficient has units of cm^{-1}, while intensity and transmitted intensity are unitless quantities of "counts" or "hits" of individual x-ray photons. As mentioned, the Beer–Lambert law describes attenuation of monochromatic x-ray photons; however, a polychromatic x-ray source was utilized here. Polychromatic x-ray photon beams undergo beam hardening [31] during interactions with the specimens as all elements and compounds preferentially attenuate lower energy x-ray photons [33], resulting in an increase in the average energy (or "hardening") of the x-ray photon beam. To account for this discrepancy, the linear attenuation coefficient, μ in Eq. (1) must be replaced by the effective attenuation coefficient, μ_{ef} [22,23] as shown in Eq. (2).

$$I = I_0 \cdot e^{-\mu_{ef} \cdot t} \tag{2}$$

The effective attenuation coefficient, μ_{ef}, which accounts for beam hardening effects, must be directly measured and varies with the thickness of the material (and likely with varying x-ray sources due to changes in x-ray photon spectra).

Commonly, x-ray experiments to track conditional changes in a material (i.e., moisture conditions or, in this case, content of corrosion products) are described as the composite system illustrated in Fig. 3 (b) [19,20,22,23,27–29]. The composite system consists of a non-corroded, saturated reinforced mortar specimen with thickness, t_m in series with corrosion products with thickness, t_{cp}. Based on Eq. (2), the transmitted intensity of the polychromatic x-ray source before reinforcement corrosion, I_{non} is described by Eq. (3):

$$I_{non} = I_0 \cdot e^{-\mu_{ef,m} \cdot t_m} \tag{3}$$

where $\mu_{ef,m}$ is the effective attenuation coefficient of mortar. The transmitted intensity of polychromatic x-ray beam before reinforcement corrosion, I_{non} continues and interacts with the corrosion products. The corrosion products further reduce the transmitted intensity as described by Eq. (4):

$$I_{corr} = I_{non} \cdot e^{-\mu_{ef,cp} \cdot t_{cp}} = I_0 \cdot e^{-\mu_{ef,m} \cdot t_m - \mu_{ef,cp} \cdot t_{cp}} \tag{4}$$

where I_{corr} is the transmitted intensity after corrosion, and $\mu_{ef,cp}$ is the effective attenuation coefficient of the corrosion product.

The change in concentration of corrosion products in the specimen, Δc_{cp} (g/cm^3) is calculated as change in corrosion products within the specimen volume or, assuming a constant cross-section, a change in corrosion products within the specimen thickness according to Eq. (5):

$$\Delta c_{cp} = \frac{\rho_{cp} \cdot \Delta V_{cp}}{V} = \frac{\rho_{cp} \cdot \Delta t_{cp}}{t} \tag{5}$$

where ρ_{cp} is the density of the corrosion products (g/cm^3), ΔV_{cp} is the change in volume of corrosion products within the specimen's volume, V, and Δt_{cp} is the change in thickness of corrosion products within the specimen's thickness, t.

Combining Eqs. (4) and (5) yields Eq. (6), which relates the transmitted intensity after corrosion, I_{corr} to the change in concentration of corrosion products, Δc_{cp}:

$$I_{corr} = I_{non} \cdot e^{-\left(\mu_{ef,cp} \cdot \Delta c_{cp} \cdot t\right)/\rho_{cp}} \tag{6}$$

and solving for change in concentration of corrosion products, Δc_{cp} (g/cm^3) yields Eq. (7):

$$\Delta c_{cp} = -\frac{\rho_{cp}}{\mu_{ef,cp} \cdot t} \cdot ln\left(\frac{I_{corr}}{I_{non}}\right). \tag{7}$$

The transmitted intensity prior to corrosion, I_{non} is a specimen's initial non-corroded condition, while I_{corr} was measured at various times after application of a constant current. Therefore, by measuring I_{corr} over time and using Eq. (7) the concentration of corrosion products can be directly measured as a function of time and two dimensional space (i.e., x-ray camera provides location-dependent information), if $\mu_{ef,cp}$ and ρ_{cp} are known. The following section describes methods to determine $\mu_{ef,cp}$, while values for ρ_{cp} are available in the literature [32].

3.2.4. Attenuation coefficients of potential corrosion products

Linear attenuation coefficient of corrosion products, μ_{cp} can be determined via calculations using tabulated data on the linear

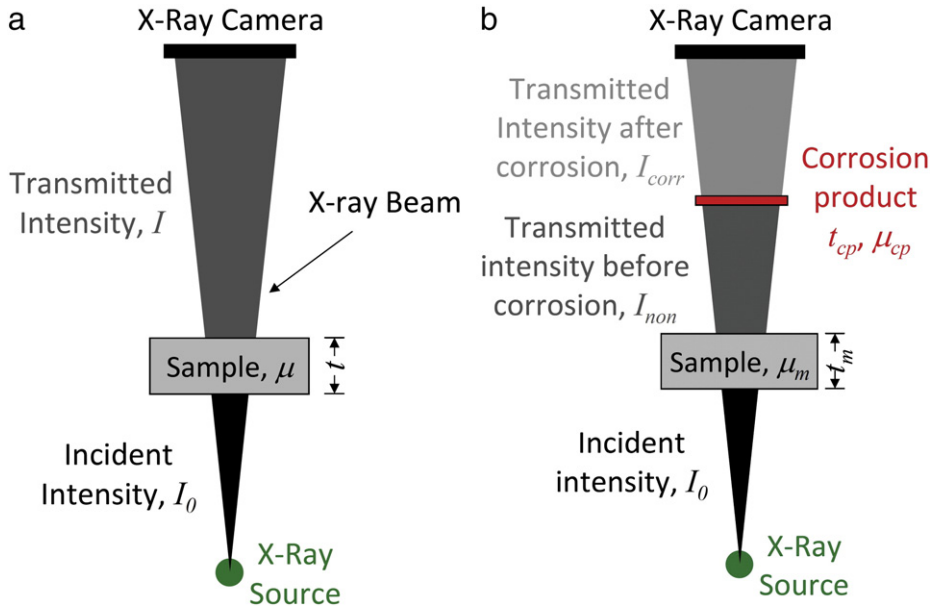

Fig. 3. Fundamental explanation of use of x-ray attenuation measurements: (a) Schematic description of Beer–Lambert law (Eq. 1) and (b) effect of change in concentration of corrosion products on x-ray attenuation measurements as described by a composite of the initial specimen and a thickness of corrosion products representing reinforcement corrosion.

attenuation coefficients of elements presented in Ref. [33]. For direct measurements of the effective attenuation coefficient, red rust (i.e., Fe_2O_3) was collected, pulverized using a mortar and pestle, and placed and compacted in acrylic containers in varying thicknesses (0, 1, 3, and 5 mm). As shown in Fig. 2, the acrylic containers were placed in front of the reference sample and the transmitted intensities were measured at varying x-ray source voltage settings (70, 80, 90, 100, and 110 keV) with the containers empty and then filled with corrosion products. The effective attenuation coefficient of the corrosion products, $\mu_{ef,cp}$ can then be calculated in accordance with Eq. (4). The same procedure is used to determine the effective attenuation coefficient of water in other investigations [20,23]. All measurements were taken with an x-ray source current setting of 75 μA. Also, the linear attenuation coefficients of compounds can be calculated as described in Ref. [33] and previously applied in Ref. [23,27] based on compound density and stoichiometry. Linear attenuation coefficients of several potential corrosion products (Fe_2O_3, Fe_3O_4, $Fe(OH)_2$, $Fe(OH)_3$, and $FeCl_2^+$) [34] and water (H_2O) were calculated.

4. Experimental results

4.1. Attenuation coefficients of corrosion products and measurement resolution

Fig. 4 shows the calculated linear attenuation coefficients for water and various thermodynamically feasible reinforcement corrosion products, determined as described in Section 3.2.4. The measured effective attenuation coefficients for Fe_2O_3 correlate well with calculated values of the linear attenuation coefficient. The linear attenuation coefficients of the various corrosion products are, in most cases, over an order of magnitude higher than that of water. Therefore, according to Eq. (1), corrosion products (which are also more dense than water, see Table 1) are more effective at attenuating x-rays than water. Of the various corrosion products considered, Fe_3O_4 has the highest linear attenuation coefficients followed by Fe_2O_3, $Fe(OH)_3$, $Fe(OH)_2$, and $FeCl_2^+$. EDS and XRD measurements performed on the mortar adjacent to the steel bar confirmed the presence of either Fe_2O_3 or Fe_3O_4.

According to Eq. (8) [22], the change in concentration corresponding to the attenuation of a single x-ray photon (concentration resolution, $R_{\Delta c}$) of the x-ray attenuation measurement is controlled by the effective attenuation coefficient (for polychromatic x-ray sources) and density of a substance, x moving within a porous material:

$$R_{\Delta c} = -\frac{\rho_x}{\mu_{ef,x}\cdot t}\cdot ln\left(\frac{I_{non}-1}{I_{non}}\right) \quad (8)$$

where ρ_x is the density of a substance x, $\mu_{ef,x}$ is the effective attenuation coefficient of a substance x, and I_{non} is the transmitted intensity from the initial, non-corroded specimen. Table 1 provides the density, linear attenuation coefficients (and measured effective attenuation coefficient of Fe_2O_3) at 80 keV, and the concentration resolution for water and the various corrosion products considered. Linear attenuation coefficients were used to calculate concentration resolutions due to the good correlation between the linear and effective attenuation coefficients of Fe_2O_3; however, effective attenuation coefficients should be measured and utilized when other corrosion products are anticipated. For Fe_2O_3, both linear and effective

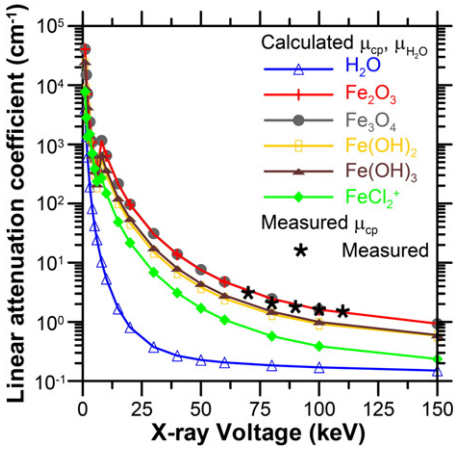

Fig. 4. X-ray attenuation spectra for water (H_2O) and various thermodynamically feasible corrosion products. The black stars indicate measured values of the effective attenuation coefficient for corrosion products.

Table 1
Density (ρ), linear attenuation coefficients (μ, at 80 keV), and concentration resolution ($R_{\Delta c}$) for various substances.

Substance	ρ [g/cm^3]	μ [cm^{-1}]	$R_{\Delta c}$ [mg/cm^3]
Water	1.00	0.184	0.599
Fe_2O_3	5.24	2.447 (2.142)[b]	0.235 (0.269)
Fe_3O_4	5.17	2.466	0.230
$Fe(OH)_2$	3.40	1.484	0.252
$Fe(OH)_3$	3.40	1.343	0.278
$FeCl_2^+$	1.39[a]	0.574	0.266

[a] Density given for tetrahydrate, which is green in color [32].
[b] Values in parentheses are measured effective attenuation coefficient (μ_{ef}, at 80 keV) and corresponding resolution.

attenuation coefficients (at 80 keV) and the resulting concentration resolutions are presented. For I_{non}, the average transmitted intensity from the specimen in its original, non-corroded condition was used. For the x-ray energy used (μ_x and I_{non} vary with x-ray energy), $R_{\Delta c}$ of water was 0.599 mg/cm^3, while $R_{\Delta c}$ enhanced to between 0.230 mg/cm^3 and 0.278 mg/cm^3 for the various corrosion products. Based on Eq. (8) and Table 1, concentration resolution is inherently improved (over that of water) when monitoring reinforcement corrosion products.

4.2. Image analysis of x-ray attenuation measurements

Fig. 5 in the electronic version of this paper (5-EV, see link in Appendix A.) is compiled videos consisting of calculated x-ray images of change in concentration of corrosion products (i.e., Eq. 7) between 3 and 147 hours of accelerated corrosion testing. Each image is identified by a sequence number and the time passed after initiation of accelerated corrosion testing in the bottom left corner in both videos. In Fig. 5(a)-EV the first several frames of the video highlight specimen details including the rebar, mortar and a size scale. Throughout the video duration in Fig. 5(a)-EV additional details and phenomena are pointed out and labeled as they appear, including corrosion products (light gray to white in color), initiation and propagation of cracks (dark gray to black in color), the probable filling of an entrapped pore with corrosion products, and excessive corrosion-induced deformations of the mortar. The video in Fig. 5 (b)-EV consists of the same images; however, with an increased frame rate and without pauses. The higher frame rate more clearly shows the excessive corrosion-induced deformations of the mortar. Deformation of a part of the specimen induces measurement distortions as the pixel dependent initial transmitted intensity, I_{non} no longer accurately coincides with the transmitted intensity after corrosion, I_{corr}. As seen most clearly after 127 hours (image 75) in both videos, excessive deformations (and resulting measurement distortion) give the appearance of corrosion products being deposited relatively far from the rebar surface.

Fig. 5 in the printed version of this paper (5-PV), is calculated x-ray images (i.e., Eq. 7) after (a) 14 and (b) 147 hours of accelerated corrosion testing. The image highlights the location of corrosion products (light gray to white in color) and cracks (dark gray to black in color). Fig. 5(a)-PV clearly shows that an initial crack has formed along with the location and amount of corrosion products required to induce the crack. Fig. 5(b)-PV shows that substantially more corrosion products have formed after 147 hours at the interface of the concrete and steel, both increasing the size of the initial crack and inducing a second crack. Additionally, as discussed above, excessive movement of the mortar and the resulting measurement distortion are most clearly visible in the top-right corner of Fig. 5(b)-PV.

Contour plots in Figs. 6 and 7 provide location-dependent information on calculated concentrations of corrosion products (Eq. 7) at various times during the accelerated corrosion testing. Fig. 6, which shows the entire x-ray image area of the measured specimen, has contours to highlight both the cracks and the concentration of corrosion products, after (a) 14 hours, (b) 71 hours, and (c) 119 hours of accelerated corrosion. The assumed type of corrosion product was Fe_2O_3, with a measured average (averaged from the varying thicknesses of corrosion product measured) effective attenuation coefficient of 2.142 cm^{-1} at 80 keV, 5.24 g/cm^3 density, and the specimen thickness was 2.0 cm. The contour plots illustrate the concentration of corrosion products in g/cm^3, which is a summation of the amount of corrosion products through the thickness of the specimen. Cracks result in negative contour values as the number of transmitted x-ray photons

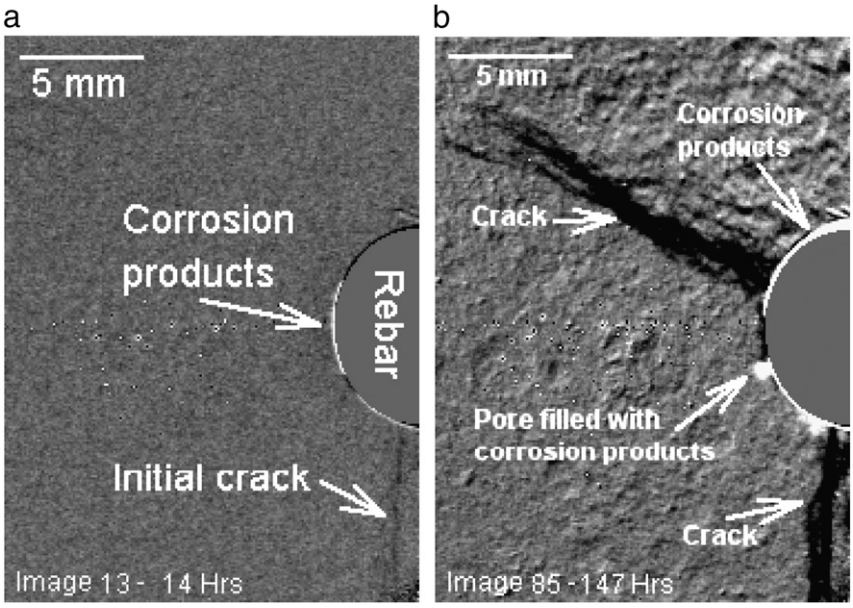

Fig. 5. (Printed version) Calculated image (i.e., Eq. 7) after (a) 14 and (b) 147 hours of accelerated corrosion testing. (Electronic version—video links in Appendix A.) Videos compiled from calculated images between 3 and 147 hours of accelerated corrosion testing (a) with various events highlighted and (b) with a higher frame rate to better illustrate corrosion-induced deformations of surrounding mortar.

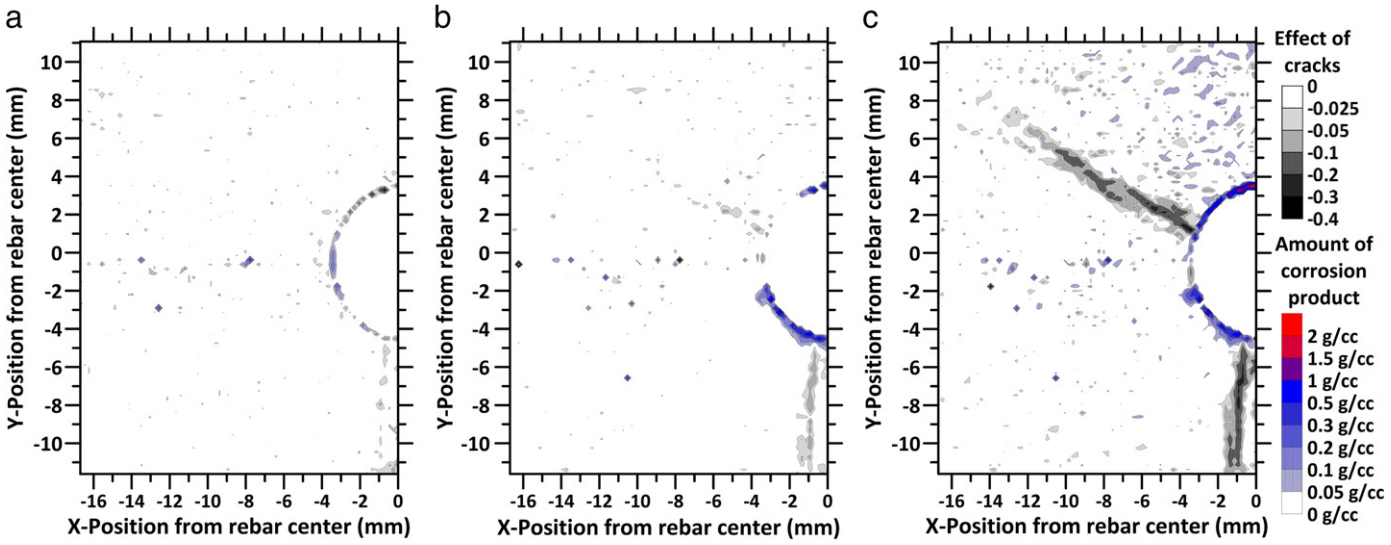

Fig. 6. Contour plots highlighting the effect of cracks on x-ray attenuation measurements and concentration of corrosion products after (a) 14 hours, (b) 71 hours, and (c) 119 hours (note: the effect of cracks is a unitless factor described by the natural log portion of Eq. 7).

increases. Fig. 7 shows a zoomed portion of the original image and excludes contours describing cracks. All contour plots are shown with units of g/cc (i.e., gram per cubic centimeter, g/cm^3).

Further detailed descriptions of Figs. 5 (for both the electronic and print versions) and 6 are included in the following sections.

4.3. Corrosion-induced cracking and deformation behavior

The development of corrosion products, described in the following section, resulted in the formation of two cracks within the measured region and a third crack, which was observed outside of the area recorded by x-ray. Fig. 5(a)-EV indicates that the first crack begins to form below the steel after 13 hours (image 12) of accelerated corrosion testing. The effect of the first crack can begin to be seen in the contour plot shown in Fig. 6(a). Figs. 5-EV and 6(a),(b),(c) indicate the width of the initial crack continuously increased during testing.

After 57 hours (image 40) a second crack developed in the upper half of the mortar. The second crack initiated at or near the surface of the steel and propagated outward toward the mortar's surface. The second crack appears to be widest at the concrete–steel interface, with decreasing width as it extends away from the steel. Quantification of the crack width is not possible with the x-ray attenuation measurement, as the effect of cracks is averaged through the 2.0 cm thick specimen measured. During propagation of the second crack, particularly from 97 hours (image 60) to the end of the test, excessive deformation of the mortar occurred. The deformation is clearly seen in Fig. 5(b)-EV in the upper and side portion of the mortar. The mortar deformation causes distortions in calculated corrosion product concentration images (i.e., Eq. 7), which is seen most clearly in the top portion of the mortar. Values for I_{non} are specific to a particular pixel/location, and as the deformations occur the measured I_{corr} values no longer match to the original corresponding I_{non}. The influence of this distortion is clearly shown in Figs. 6(c) and 7(c), through the apparent formation of corrosion products far from the steel. These apparent formations are attributed to distortions and not the actual formation of corrosion products. The deformation of the side portion of the mortar appears to have caused separation between the mortar and the steel, as indicated in image 75 (127 hours). As this occurs, the corrosion products appear to either relocate or disappear. Most likely the corrosion products remain in place, but the effect of the crack controls the x-ray attenuation measurement results in such a damaged specimen. This, along with measurement distortions induced by excessive deformations, is a limitation of the presented approach. Also, the x-ray attenuation data are an average through the specimen thickness. Thus, if both corrosion products and a crack form at the same location, the two behaviors are averaged through the specimen thickness, potentially resulting in errant quantifications of the amount of corrosion products or qualification of the cracking behavior. However, before cracking occurs, calculated concentrations of corrosion products remain accurate.

The first and secondary crack can be seen in their final states (147 hours, image 85) in Fig. 5(b)-PV. Excessive deformation and resulting distortion of the calculated image (Eq. 7) are also apparent in Fig. 5(b)-PV.

The contour plots in Fig. 6(a),(b),(c) illustrate the effect of the cracks. In Fig. 6(a) (14 hours, image 13) the initial crack has recently formed and a line of negative contours is seen directly below the rebar. Fig. 6(b) (71 hours, image 47) indicates the initial crack has likely increased in size and connectedness, and a second crack has initiated from the steel surface. Fig. 6(c) shows both cracks have further increased in size and the impact of calculated image distortion is clearly seen in the upper portion of the mortar.

4.4. Development and location of corrosion products

Fig. 5(a)-EV shows corrosion products were clearly detected at the concrete–steel interface after 9 hours (image 8) of accelerated corrosion testing. Initially, the corrosion products formed on the side-facing surface of the steel; however, with additional time corrosion products start to form on the bottom-facing surface. After 16 hours (image 15) corrosion products begin to protrude into an entrapped void near the steel surface. Corrosion products penetrate deeper into the mortar as accelerated corrosion testing continued, and after 33 hours (image 28) corrosion products are seen on the top-facing surface of the steel. After 89 hours (image 56) additional corrosion products appear to enter the entrapped pore; however, after the second crack propagates nearly all corrosion products appear to form near the top-facing surface of the steel. This observation is quantified and verified by Figs. 7 and 8, as discussed in the following paragraph. After 127 hours (image 75), excessive deformation of the mortar above the steel occurs as corrosion products no longer appear to protrude into the mortar, but rather push the mortar out of the way.

The zoomed contour plots in Fig. 7(a), (b), and (c) quantify and summarize the information presented in Fig. 5(a)-EV. Fig. 7(a)

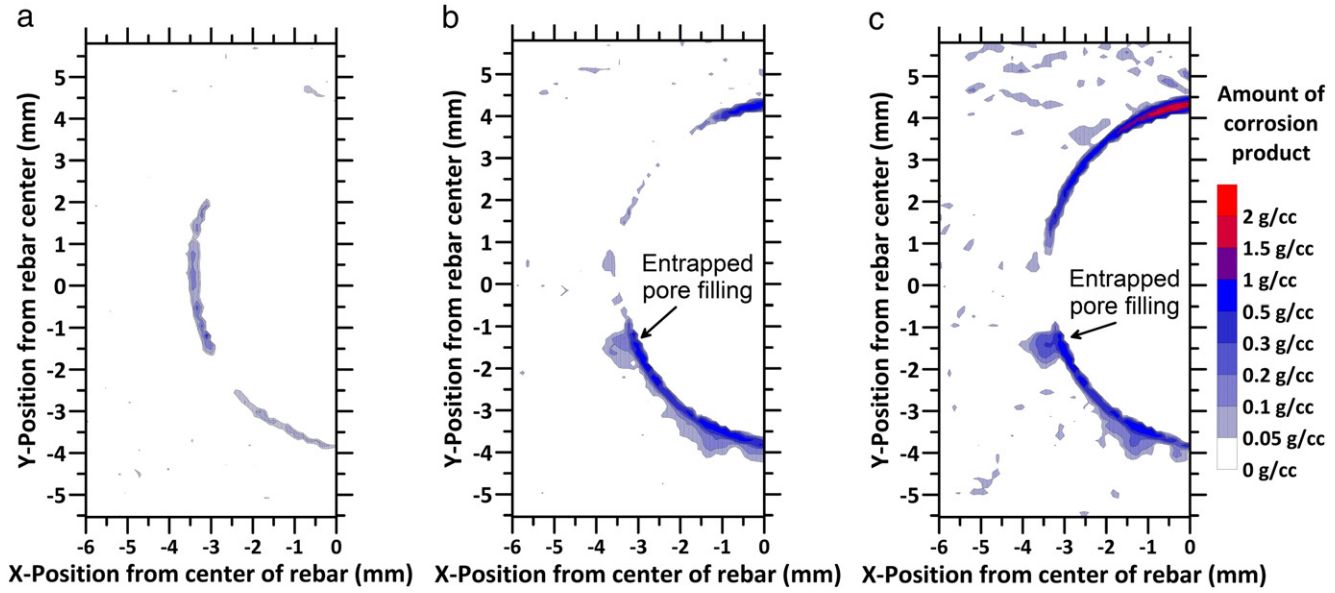

Fig. 7. Zoomed contour plots highlighting only concentration of corrosion products after (a) 14 hours, (b) 71 hours and (c) 119 hours.

indicates that concentration of corrosion product ranged up to a maximum between 0.1 and 0.2 g/cm^3 after 14 hours. The concentration of corrosion products and area where corrosion products exist increased after 71 hours (Fig. 7(b)) and the filling of the entrapped pore is clearly shown. Between 71 and 119 hours, Fig. 7(b) and (c), respectively, a great deal of additional corrosion products formed near the top-facing side of the rebar. Fig. 8 shows a contour plot of the additional corrosion products formed between 71 and 119 hours. Fig. 8 confirms that up to 1.5 g/cm^3 of corrosion product formed near the top-facing surface of the rebar, while during the same time a maximum increase of only 0.2 g/cm^3 occurred near the lower portion of the rebar.

Through further image analysis, polar transformation of results shown in Fig. 7(c) are presented in Fig. 9. Polar transformation allows plotting of the circular surface of the rebar as a flat surface, from which corrosion products protrude. The concentration of corrosion products was averaged over the radius up to 1.0 mm from the rebar surface as presented in Fig. 10. Fig. 10 illustrates concentrations of corrosion products both increase and penetrate deeper into the mortar specimen with increased time. The polar transformation also facilitates estimation of size of the CAR. In this case (where a very high corrosion-inducing current was applied), as shown by the solid circular symbol plot (13 hours) the CAR was between 0.09 and 0.18 mm. The accelerated nature of this initial test may have not provided sufficient time for realistic penetration of corrosion products into the surrounding mortar. With the presented experimental setup a single pixel of the x-ray camera corresponds to a 0.89×0.89 mm^2 area of the specimen. Previously reported values for the CAR vary between 0.002 to 0.12 mm, indicating improved spatial resolution of the x-ray images may be required.

Fig. 11(a) and (b) show an SEM image of the mortar near the concrete–steel interface and an EDS mapping of iron, calcium, and silicon in the same region, respectively. Fig. 11(b) indicates iron (i.e., corrosion products) indeed penetrated into the microstructure of the cement paste, with particular areas of increased iron content.

The concentration of corrosion products at the end of testing (147 hours, image 85) was integrated to estimate a total mass loss of the rebar due to corrosion during the test. Values for mass loss were also estimated by Faraday's law and measured through gravimetric means (i.e. weighing). Table 2 shows the various means to measure and estimated mass loss resulted in very good agreements. A 9% difference was found between weight and x-ray measurement methods. A higher discrepancy in mass loss (43%) between Faraday's law estimation and x-ray method may be explained by the assumption in Faraday's law of 100% current efficiency (meaning that all current applied is used in the electrochemical reaction to dissolve the iron). It should also be mentioned that only one half of the rebar was monitored during this testing (see Fig. 1(b)). To obtain the total mass loss from x-ray attenuation measurements, symmetry (i.e., in terms of concentration of corrosion products) was assumed.

5. Discussion of results

X-ray attenuation measurements of corrosion products are more effective (i.e., improved inherent concentration resolution) than the more common monitoring of water movements in cementitious

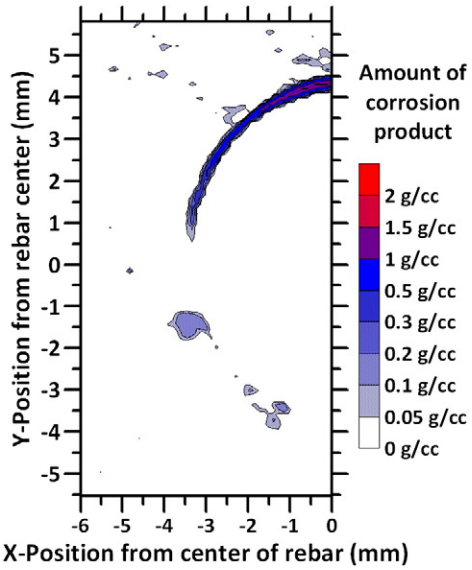

Fig. 8. Additional concentration of corrosion products between 71 hours and 119 hours of accelerated corrosion testing (i.e., Fig. 6(c) minus Fig. 6(b)).

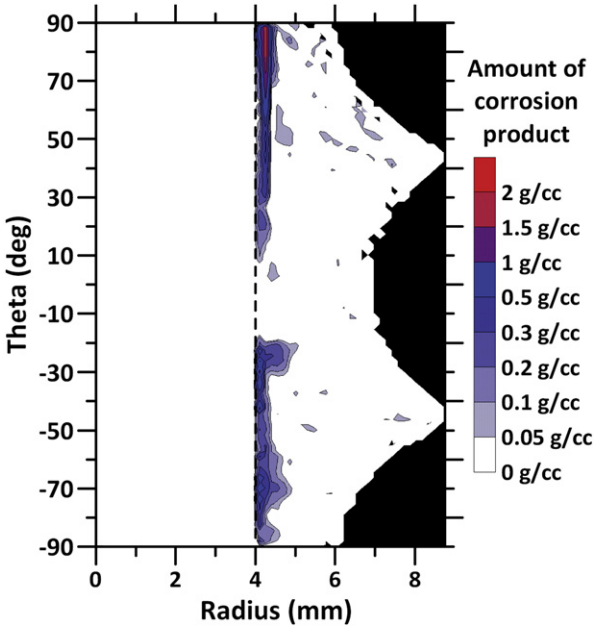

Fig. 9. Polar transformation contour plots of corrosion product concentrations after 119 hours (i.e., Fig. 6(c)).

materials. The x-ray attenuation measurement is non-destructive and does not influence the accelerated corrosion testing method. Further, the current applied to induce corrosion (i.e., accelerated corrosion method) does not appear to interact with the x-ray photons transmitted through the measurement specimen.

Corrosion-induced cracks were seen to form at or near the concrete–steel interface and propagate outward to the specimen surface (in agreement with previous model behaviors [6,13]). Further, comparisons of the development of corrosion products and the corrosion-induced cracking of the mortar specimen provided the following insights. The development of additional corrosion products appears to be linked to the degree of damage (i.e., cracking) at the interface of the steel and surrounding mortar. Prior to extensive cracking (i.e., before 71 hours, image 47) the corrosion products appear to penetrate into the pores of the mortar. However, after more extensive cracking the corrosion products appear to form between the steel and mortar, simply moving the mortar rather than penetrating into it. Additionally, as shown in Fig. 8, corrosion products appear to favor forming at the damaged interface, as nearly all additional corrosion products were seen to form in this region after 71 hours.

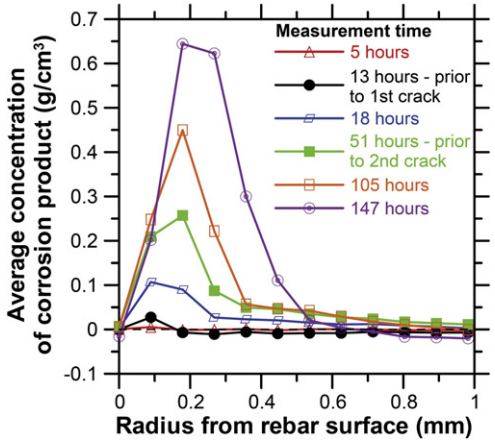

Fig. 10. Average concentration of corrosion products as a function of radius from the rebar surface at varying times (5, 13, 18, 51, 105, and 147 hours).

It is evident from the results that the x-ray attenuation method is suitable to track the time-dependent development of the corrosion products and subsequent initiation and propagation of cracks due to the expansive nature of the corrosion products. While a relatively high current was applied to induce corrosion to test the applicability of the measurement technique, results clearly indicate that corrosion products and corrosion-induced cracking under natural corrosion conditions would similarly be detected (assuming location of specimen, x-ray source, and camera is constant as discussed below). Furthermore, the experimental method allows for the determination of the actual concentration of the corrosion products averaged through the specimen thickness. Measurement distortions due to excessive deformations of the mortar occurred; however, future measurements would likely stop well before similar distortions occur. The most important information from the technique (i.e., amount and location(s) of corrosion products necessary to induce cracking) is collected well before excessive distortions are observed. Polar transformation of the x-ray images provides the average amount of corrosion products as a function of the radius (i.e., distance from rebar surface) and time prior to initiation of cracking in the reinforced mortar sample. In other words, the x-ray attenuation method can directly measure the size of the CAR as both the corrosion and the corrosion-induced cracking behaviors are monitored. Further parametric studies are needed; however the presented technique should provide unique insight on the corrosion process (including amount and location of corrosion products and time-to-cracking) under laboratory conditions, improving understanding and modeling of reinforcement corrosion and subsequent corrosion-induced concrete cracking.

The presented method could be applied for in-situ measurement of the extent of reinforcement corrosion and resulting damage; however, many practical issues would need to be considered. As seen in Fig. 5(b) and discussed previously, movement of the specimen caused measurement distortions. Therefore, positions of the x-ray source, camera, and measured area must be constant at differing measurement times. With possible measurement intervals in the range of a year or more, identical positioning may be difficult. Furthermore, effects of other various transient behaviors in concrete (e.g., moisture movements, possible leaching, etc.) on the x-ray attenuation measurements would need to be isolated or corrected. A similar, yet limited radiography technique (i.e., γ-ray imaging) has been applied for in-situ determinations of rebar location and can even estimate cross-section reductions of reinforcement due to corrosion [35]. γ-Ray imaging, identically to medical/dental radiography, detects the denser steel (analogous to bone, teeth) within the less dense concrete (analogous to human soft tissues) in a single measurement. However, radiography does not provide the necessary information to calculate concentration changes (see Eq. 7) and appears (based on results presented in Ref. [35]) unable to assess the location of corrosion products and any corrosion-induced cracking of the surrounding concrete.

6. Summary and conclusions

The applicability of x-ray attenuation measurements to monitor the development of corrosion products as well as initiation and propagation of cracks in cementitious materials was presented. Results obtained from x-ray attenuation measurements and subsequent image analyses of reinforced mortar samples tested under accelerated corrosion conditions indicate that:

1. The x-ray attenuation measurements do not affect accelerated corrosion testing and the current applied to induce corrosion does not appear to interact with x-ray photons.

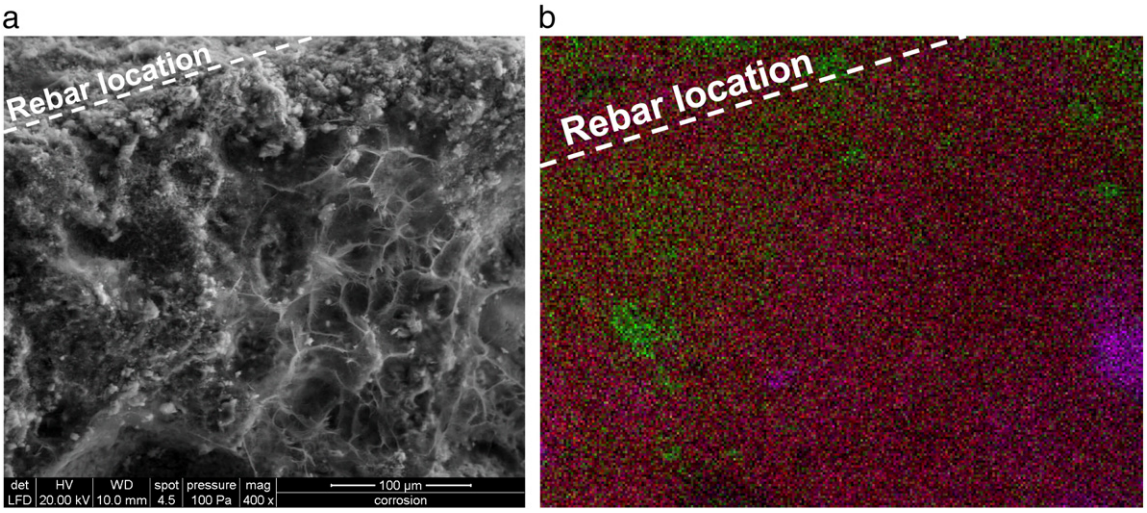

Fig. 11. (a) SEM image of mortar surrounding steel rebar with rebar location noted, (b) EDS mapping of Fe (green), Ca (red), and Si (purple) in the same area.

2. X-ray attenuation measurement allow non-destructive monitoring of corrosion products and it has been found that:
   - Similar to previous observations, corrosion products were seen to form at or near the steel surface for the corrosion conditions investigated.
   - Corrosion products initially penetrate into the mortar.
   - After excessive deformation due to corrosion-induced cracking the corrosion products appear to form between the steel and mortar, simply moving the mortar rather than penetrating into it.
3. The concentration of corrosion products can be determined as a function of time and space with the x-ray attenuation measurements.
   - The total mass loss of steel obtained by the x-ray attenuation method correlates well with determination of the mass loss by gravimetric means as well as Faraday's law.
4. Initiation and propagation of corrosion-induced cracking can be monitored.
   - Results of the x-ray attenuation measurements allow monitoring of crack initiation at or near the steel surface as well as propagation of the crack outward toward the mortar's surface.

Further detailed study is warranted into applying this method to measure the impact cracks have on moisture ingress and the subsequent reinforcement corrosion in a single test specimen (i.e., full service life). X-ray measurements provide a direct measure of the moisture ingress and corrosion behaviors, including both the location and amount of moisture and corrosion products.

Acknowledgements

The first author gratefully acknowledges the financial support of Taumoses Legat as well as Femern Bælt A/S, Sund & Bælt Holding A/S and The Danish Agency for Science, Technology and Innovation. Financial contributions from the Danish Expert Centre for Infrastructure Constructions are also greatly appreciated. Furthermore, the authors acknowledge the assistance of Adéla Peterová.

Table 2
Comparison of mass loss obtained by different measurement techniques. Deviation from x-ray determination shown.

Test method	Mass loss [g]	Deviation [%]
Faraday's law	0.19	43
X-ray attenuation	0.11	–
Weighing	0.12	9

Appendix A. Supplementary data

Supplementary data to this article can be found online at doi:10.1016/j.ydbio.2011.06.020.

References

[1] J. Gulikers, M. Raupach, Numerical models for the propagation period of reinforcement corrosion—comparison of a case study calculated by different researchers, Materials and Corrosion 57 (8) (2006) 618–627.
[2] O.B. Isgor, A.G. Razaqpur, Modelling steel corrosion in concrete structures, Materials and Structures 39 (287) (2006) 259–270.
[3] A. Michel, M. Geiker, H. Stang, J. Olesen, Numerical modelling of reinforcement corrosion in concrete structures, Proceedings of the 8th fib PhD Symposium, Kgs. Lyngby, Denmark, 2010.
[4] C. Alonso, C. Andrade, J. Rodriguez, J.M. Diez, Factors controlling cracking of concrete affected by reinforcement corrosion, Materials and Structures 31 (211) (1998) 435–441.
[5] Z. Bažant, Physical model for steel corrosion in concrete sea structures—application, Journal of the Structural Division 105 (1979) 1155–1166.
[6] F.J. Molina, C. Alonso, C. Andrade, Cover cracking as a function of rebar corrosion: part 2—numerical model, Materials and Structures 26 (9) (1993) 532–548.
[7] L. Chernin, D.V. Val, K.Y. Volokh, Analytical modelling of concrete cover cracking caused by corrosion of reinforcement, Materials and Structures 43 (4) (2010) 543–556.
[8] Y. Liu, R. Weyers, Modeling the time-to-corrosion cracking in chloride contaminated reinforced concrete, ACI Materials Journal 95 (6) (1998) 675–681.
[9] T. El Maaddawy, K. Soudki, A model for prediction of time from corrosion initiation to corrosion cracking, Cement and Concrete Composites 29 (3) (2007) 168–175.
[10] S. Caré, Q. Nguyen, V. L'Hostis, Y. Berthaud, Mechanical properties of the rust layer induced by impressed current method in reinforced mortar, Cement and Concrete Research 38 (8–9) (2008) 1079–1091.
[11] C.-Q. Li, Y. Yang, R.E. Melchers, Prediction of reinforcement corrosion in concrete and its effects on concrete cracking and strength reduction, ACI Materials Journal 105 (1) (2008) 3–10.
[12] K. Noghabai, FE-modelling of cover splitting due to corrosion by use of inner softening band, Materials and Structures 32 (221) (1999) 486.
[13] S.F.U. Ahmed, M. Maalej, H. Mihashi, Cover cracking of reinforced concrete beam due to corrosion of steel, ACI Materials Journal 104 (2) (2007) 153–161.
[14] E. Bohner, H. Müller, S. Bröhl, Investigations on the mechanism of concrete cover cracking due to reinforcement corrosion, FraMCos-7—7th International Conference on Fracture Mechanics of Concrete and Concrete Structures, Jeju, Korea, 2010.
[15] D.V. Val, L. Chernin, M.G. Stewart, Experimental and numerical investigation of corrosion-induced cover cracking in reinforced concrete structures, Journal of Structural Engineering 135 (2009) 376–385.
[16] I. Petre-Lazar, Aging assessment of concrete structures submitted to steel corrosion, Ph.D. thesis, Laval University, Quebec, Canada, (in French) (2000).

[17] Y. Kawasaki, Y. Tomoda, M. Ohtsu, AE monitoring of corrosion process in cyclic wet–dry test, Construction and Building Materials 24 (12) (2010) 2353–2357 special Issue on Fracture, Acoustic Emission and NDE in Concrete (KIFA-5).
[18] D. Aggelis, E. Kordatos, D. Soulioti, T. Matikas, Combined use of thermography and ultrasound for the characterization of subsurface cracks in concrete, Construction and Building Materials 24 (10) (2010) 1888–1897.
[19] P.H. Baker, D. Bailly, M. Campbell, G.H. Galbraith, R.C. McLean, N. Poffa, C.H. Sanders, The application of x-ray absorption to building moisture transport studies, Measurement 40 (9–10) (2007) 951–959.
[20] K. Hansen, S. Jensen, L. Gerward, K. Singh, Dual-energy x-ray absorptiometry for the simultaneous determination of density and moisture content in porous structural materials, Proceedings of the 5th Symposium on Building Physics in the Nordic Countries, Vol. 1, Gothenburg, Sweden, 1999, pp. 281–288.
[21] J. Hu, P. Stroeven, X-ray absorption study of drying cement paste and mortar, Cement and Concrete Research 33 (3) (2003) 397–403.
[22] S. Roels, J. Carmeliet, Analysis of moisture flow in porous materials using microfocus x-ray radiography, International Journal of Heat and Mass Transfer 49 (25) (2006) 4762–4772.
[23] G. Sant, J. Weiss, Using x-ray absorption to assess moisture movement in cement-based materials, Journal of ASTM International 6 (9) (2009) 1–15.
[24] DS/EN 197-1 Cement—part 1: composition, specification and conformity criteria for common cements, 2001 29 pp.
[25] DS-2426, Concrete—materials—rules for application EN 206-1 in Denmark, Tech. rep, Danish Standards Association, 2004.
[26] www.gni.dk GNI X-ray System, Technical University of Denmark, 2010.
[27] B. Pease, Influence of concrete cracking on ingress and reinforcement corrosion, Ph.D. thesis, Technical University of Denmark, Kgs. Lyngby, Denmark (December 2010).
[28] B. Pease, J. Couch, M. Geiker, H. Stang, J. Weiss, Assessing the portion of the crack length contributing to water sorption using x-ray absorption measurements on concrete wedge splitting specimens, ConcreteLife'09: Second International RILEM Workshop on Concrete Durability and Service Life Planning, Haifa, Israel, 2009.
[29] M. Pour-Ghaz, F. Rajabipour, J. Couch, J. Weiss, Numerical and experimental assessment of unsaturated fluid transport in saw-cut (notched) concrete elements, ACI SP 266—Modeling as a Solution to Concrete Problems, American Concrete Institute, 2009, pp. 73–83.
[30] G. Knoll, Radiation Detection and Measurement, J. Wiley, 1989.
[31] R.A. Brooks, G.D. Chiro, Beam hardening in x-ray reconstructive tomography, Physics in Medicine and Biology 21 (3) (1976) 390–398.
[32] P. Patnaik, Handbook of Inorganic Chemicals, McGraw-Hill, 2003.
[33] J. Hubbell, S. Seltzer, Tables of x-ray mass attenuation coefficients and mass energy-absorption coefficients, Tech. Rep. NISTIR 5632, National Institute of Standards and Technology, Maryland, USA, 2004.
[34] A. Küter, Management of reinforcement corrosion: A thermodynamical approach, Ph.D. thesis, Technical University of Denmark, Kgs. Lyngby, Denmark (April 2009).
[35] M.A. Mariscotti, F. Jalinoos, T. Frigerio, M. Ruffolo, P. Thieberger, Gamma-ray imaging for void and corrosion assessment—safety and utility of the technology make it appropriate for field application, Concrete International 31 (11) (2009) 48–53.